Dynamics of High Molecular Weight Cylindrical and Lamellar Block Copolymers with X-ray Photon Correlation Spectroscopy (XPCS)

Omar Taleb[a,b], Patrick Blatt[a,b], Virginia Signorini[c], Onyekachi Oparaji[d], Kyougmin Kim[e], Eric Lochner[f], Suresh Narayanan[g], Qingteng Zhang[g], Daniel Hallinan Jr.[a,b,*]

[a] Department of Chemical and Biomedical Engineering, Florida A&M University-Florida State University College of Engineering, Tallahassee, FL 32310, USA

[b] Aero-propulsion, Mechatronics, and Energy Center, Florida A&M University-Florida State University College of Engineering, Tallahassee, FL 32310, USA.

[c] Department of Civil, Chemical, Environmental and Materials Engineering (DICAM)—Alma Mater Studiorum, University of Bologna, Via Terracini 28, Bologna 40131, Italy

[d] Intel Corporation, Hillsboro, OR 97124, USA.

[e] Storagenergy Technologies Inc., Salt Lake City, UT 84104, USA.

[f] Physics Department, Florida State University, Tallahassee, FL 32304, USA.

[g] Advanced Photon Source, Argonne National Laboratory, Lemont, IL 60439, USA.

[*]Author to whom correspondence should be addressed, dhallinan@eng.famu.fsu.edu

Abstract

The structure and dynamics of polystyrene-b-poly(ethylene oxide) (PS-b-PEO) block copolymers (BCPs) were studied. The BCPs exhibited microphase separated cylindrical and lamellar morphologies. Structural dynamics were measured with X-ray photon correlation spectroscopy (XPCS) in the small-angle regime. Morphologies and domain sizes were evaluated using small angle x-ray scattering (SAXS), scanning electron microscopy, and atomic force microscopy. Different solvent processing conditions were investigated. Grain sizes evaluated using SAXS were found to depend on processing only for the rubbery majority BCP. The structural relaxation times were examined as a function of PS volume fraction, temperature, morphology, and structural sizes. Well above the glass transition temperature (T_g) of PS, all samples exhibited stretched autocorrelation decays and diffusive dynamics. Near T_g of PS the dynamics of all samples was anomalous with compressed autocorrelation decays and hyperdiffusive dynamics. This transition occurred at 153 °C or 1.13T_g of PS. In the diffusive regime (at high temperature), structural relaxation times were dependent on the processing method. Near PS T_g (at low temperature), structural relaxation times scaled with the PS volume fraction. Structural relaxation times do not correlate with grain size, indicating that the out-of-equilibrium state of PS dominates structural dynamics of these strongly phase segregated BCPs.

Keywords

diblock copolymer; morphology; rubbery; glassy; out-of-equilibrium

I. Introduction

Nanostructured polymer materials (NPMs) are composed of two or more phases with at least one characteristic dimension less than 100 nm. They have exhibited unprecedented decoupling of macroscopic material properties such as mechanical strength and ionic conductivity, particularly in block copolymer (BCP) and polymer nanocomposite electrolytes.[1-13] To date, the underlying causes of this decoupling are not well understood. Interfacial effects associated with tethering and/or confinement could be responsible for modifying the properties of the individual components in NPMs.[14, 15] On the other hand, properties like low-frequency elasticity can emerge from the structure itself.[16] Therefore, design of advanced NPMs requires a fundamental understanding of material behavior at several length scales from nanometer to macroscopic, linked by mesoscopic structure and dynamics.

One class of NPMs are high-molecular-weight BCPs that tend to form tough membranes with mechanical strength sufficient for battery[4] and membrane-separation applications.[17, 18] These materials resist lithium dendrites, opening the possibility for safer, longer-range electric vehicles, but they suffer from low ionic conductivity, which limits the battery discharge rate. Similarly, BCP membranes can combine selective transport and mechanical strength at temperatures and pressures that cannot be achieved with homopolymer membranes. Membrane separations are energy-efficient means to generate fresh water and capture carbon dioxide. Higher generation rates and longer membrane lifetimes would make membrane separations cost competitive with energy intensive technologies. While BCP membranes have the potential to improve the sustainability of our energy and water technologies, the problem of low transport must be addressed without adversely affecting mechanical strength.

BCPs comprise two or more polymers covalently attached at their chain ends. Under certain conditions, they microphase segregate into predictable nanoscale structures, also called morphologies. The fundamental repeat distance is called the domain size, and distance over which the repeating structure is oriented is termed the grain size. In bulk samples prepared in the absence of a directing field, each grain is randomly oriented. A schematic of randomly oriented lamellar planes is shown in the middle pane of Figure 1. Morphology is dictated primarily by BCP composition, but it and grain structure can be significantly affected by processing.[19-31] A possible solution to improving transport in BCP membranes is to use the grain structure and dynamics to further decouple transport from mechanical properties.[32, 33] In order to achieve this, the connection of grain dynamics (mesoscale) to local segmental motions and to application-specific macroscopic material properties must be understood.

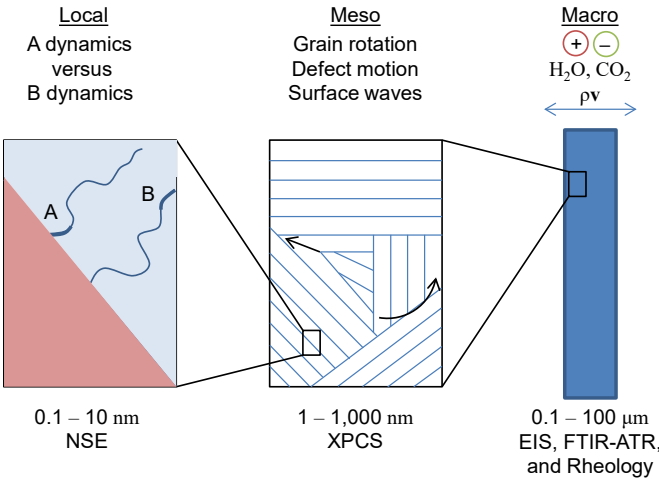

Figure 1. Schematics (from right to left) of dynamics in a lamellar block copolymer across decreasing length scales. Ionic conductivity, molecular diffusion, and mechanical response are measured at macroscopic length scales using, for example, electrochemical impedance spectroscopy (EIS), Fourier transform infrared – attenuated total reflectance (FTIR-ATR) spectroscopy, and rheology. Mesoscopic dynamics of grains are interrogated with, for example, X-ray photon correlation spectroscopy (XPCS). Local polymer segmental dynamics are evaluated with, for example, neutron spin echo (NSE) spectroscopy of selectively deuterated samples.

The microstructure of BCPs and dynamics in unstructured polymers are both relatively well established.[34, 35] Significant efforts have revealed the macroscopic mechanical response of well-ordered BCPs.[16] An understanding of the impact of nanostructure on local motion of untethered polymer chains is beginning to emerge.[15, 36, 37] However, only limited effort has been dedicated to understanding dynamics in strongly segregated BCPs, especially on length scales comparable to the size of the nanostructures. High-molecular-weight BCPs are strongly segregated with sharp interfaces that are conducive to the study of local dynamics. As will be shown in this work, they do however form poorly ordered morphologies due to kinetic constraints related to the inability of highly entangled BCPs to closely approach an ideal state on the experimental time frame available for processing/self-assembly. Thus, beautiful micrographs of large-grain morphologies regularly shown (and often expected) in studies of low-molecular-weight BCPs are not possible with high-molecular-weight BCPs, nor is it possible to unequivocally define their morphology in some cases. Despite this drawback, the study of these out-of-equilibrium materials is important due to their superiority in the aforementioned applications. In addition to battery[4] and membrane-separation applications,[17, 18, 38] block copolymers enable innovation in a diversity of other interesting applications such as thermoplastic elastomers,[39] nanolithography,[19] supercapacitors,[40] electro- or photo-catalysis,[41] and solar cells.[42]

High-molecular-weight BCPs exhibit the highest ionic conductivity that has been observed in BCP electrolytes.[2] They also have minimal microphase mixing, which plays a role in macroscopic properties such as ionic conductivity.[43, 44] Sharp interfaces in strongly segregated BCPs are expected to play a particularly pronounced role in macroscopic properties of high contrast BCPs. High contrast can refer to mechanical properties, as is the case in thermoplastic elastomers in which one microphase is glassy and another is rubbery. It can also refer to transport properties, as is the case in amphiphilic BCPs in which

one microphase is selective to hydrophilic and ionic species and another is hydrophobic. In all these situations the continuity of the microphases within a grain and across grain boundaries can dramatically impact the resulting macroscopic properties.[45] This would be most important when the domain and grain structures are static or evolve on time scales much longer than the relevant transport time scale. Domain and grain connectivity would be least important if the structures fluctuate rapidly with respect to transport. In essentially all applications mentioned above, BCP properties of importance depend on dynamics. This work examines high contrast, strongly phase segregated BCPs of poly(ethylene oxide) (PEO) and polystyrene (PS). PEO is a rubbery, hydrophilic polymer that selectively sorbs water and carbon dioxide, as well as coordinating alkali metal cations such as lithium. PS is a hydrophobic, glassy polymer that provides mechanical strength. Grains are randomly oriented within the BCP, but both lamellae and cylinders are continuous within domains and across grain boundaries.[46, 47] Therefore, high molecular weight BCPs with volume fractions predicted to form these morphologies are the focus of the present study.

Experimentally, it is quite challenging to investigate mesoscopic dynamics in nanostructured materials. Spectroscopic techniques primarily probe the molecular scale. Significant effort has been committed to measuring heterogeneous dynamics in amorphous glasses, which appear to be limited to length scales below about 3 nm and have no clear connection to the heterogeneous structure.[48, 49] Rheology on the other hand measures bulk response that can provide information over a wide frequency range but is not specific to the structural length scale. Scattering techniques are able to span the length scale between spectroscopy and rheology. XPCS is appropriate for our intended investigation because it is sensitive to time-resolved changes of structure.

Rheology and dielectric spectroscopy have been used to characterize the dynamics of BCPs. These techniques are limited, because they measure the response of all molecules in the system due to an applied external field. It is difficult to isolate the contribution of an individual process to the overall response, where the collection of inter- and intramolecular relaxation is very large when the system is formed of an aggregated structure such as lamellar, cylindrical, or micellar components.[50] Dynamics of the mesostructure can be more directly probed with XPCS, which is a powerful technique to measure the dynamics in a wide range of different materials. The dynamic structure factor measured by XPCS quantifies relaxation time as a function of the scattering vector, q. The compatibility with optically opaque samples is one advantage of XPCS compared to light scattering techniques.[51] Moreover, light scattering techniques are usually sensitive to spatial variation with a length scale above 100 nm, whereas the sensitivity of XPCS can be commensurate with or below the sub-nm wavelength of the hard x-ray beam.[52-54] Small angle x-ray scattering (SAXS) collected during XPCS measurements can be used to investigate block copolymer morphology, grain size, and crystallinity as a function of processing conditions. This is complemented with scanning electron microscopy (SEM) and atomic force microscopy (AFM) to determine BCP structure in real space.

In our previous study, we characterized block copolymer electrolyte structure as a function of salt concentration and temperature.[52] In addition, we studied viscoelasticity and structural dynamics with rheology and XPCS, respectively. Although the salt concentration had a significant effect on structure by increasing the volume fraction of the rubbery phase, it did not significantly affect the dynamics measured by XPCS. The only effect on viscoelasticity was due to changes in structure. Balsara, Watanabe and coworkers studied ordering kinetics of a much lower molecular weight (33 kg/mol) BCP of PS cylinders in a polyisoprene (PI) matrix,[50] and Bates, Mahanthappa, and coworkers examined both grain growth and

structural relaxation (attributed to grain rotation) in a low molecular weight (29 kg/mol) BCP of polybutadiene (PB) spheres in a PS matrix.[55] There have not been any studies on the same chemistry spanning multiple morphologies and glassy phase volume fractions, which is the focus of this work. The fact that structural dynamics were observed in neat BCPs by XPCS was somewhat unexpected, due to the prediction that the microstructure of a strongly segregated BCP leads to low frequency rheological response that is different from terminal flow of homopolymers and liquids.[56-58] This was perhaps a naïve expectation considering the various reports of different relaxation modes of ordered BCPs.[59-61] This paper studies the structure and dynamics of polystyrene-b-poly(ethylene oxide) (PS-b-PEO) of lamellar and cylindrical morphologies as a function of processing conditions. The structure is evaluated using SAXS, SEM, and AFM, where the grain size is controlled by solvent vapor annealing. The purpose of the work is to gain fundamental understanding of the physical phenomena underpinning the structural dynamics that have been observed and to examine the impacts of temperature, structural dimensions, morphology and PS volume fraction.

II. Experimental Section

In this work, one type of BCP chemistry, PS-b-PEO, with three different phase volume fractions were studied. They are termed SEO-E, SEO-C, and SEO-I. All three samples were synthesized using anionic synthesis as described previously.[62] The polystyrene volume fraction at 90 °C (ϕ_{PS}), number average molecular weight (M_n) of each block and dispersity ($Đ$) are reported in Table 1. SEO-E and SEO-C are well-paired SEO BCPs with approximately 140 kg/mol total M_n and approximately 30 vol% minority phase. With a χN of greater than 60, both these polymers are predicted to form hexagonally packed cylinders by theoretical predictions for neutral symmetric BCPs. SEO-I has a larger total M_n of more than 250 kg/mol and less than 60 vol% PS, placing it well within the predicted lamellar morphology of the strongly phase segregated BCP phase diagram.[34, 63] Although the total M_n is not as well matched with the other two polymers, it was the most appropriate lamellar BCP available in our inventory of custom polymers.

Table 1. Molecular weights of PS and PEO blocks in each sample studied in this paper.

Block copolymer	ϕ_{PS}	$M_n(PS)^*$	$M_n(PEO)^*$	Đ
SEO-E	0.28	36.5	104	1.05
SEO-C	0.7	91.5	43.7	1.10
SEO-I	0.58	149	117	1.06

*Units is [kg/mol]

To prepare membranes and study the effect of evaporation rate on grain size, approximately 1 g of SEO was dissolved in approximately 10 mL of toluene in an air environment. The mixture was stirred at 700 RPM for an hour at 65 °C resulting in a clear and homogeneous solution. The solution was transferred to 2 stainless steel dishes of diameter 75 mm (VWR, model BOCH8636), each containing 5 mL. Casting was conducted under two different conditions. The first method involved high evaporation rate that is open to a nitrogen atmosphere, denoted OA, while the other method used a lower evaporation rate achieved by covering the stainless-steel casting dish, denoted UD, thus allowing only a small gap for solvent vapor to escape. The solutions were maintained at 80 °C with a nitrogen purge for one week to allow solvent to evaporate. Based on visual observation, most solvent evaporated in 1 hr for OA and in 48 hr for UD. Samples from both processing methods were kept in the casting oven for one week to maintain the same thermal history. The dry membranes were removed from the dishes and dried under vacuum at 90 °C for 48 hours. The thickness of the as-cast membranes was around 40 μm, but XPCS requires a thickness of 1 to 2 mm. To reach this requirement, each membrane was folded multiple times and pressed at 115 °C in a dry room (dew point -23°F, ambient T 71°F) using a Carver hot press applying a force of 1.6 MTon (equivalent to 1000 psi) for approximately 5 minutes. The thickness of the pressed membrane was checked to make sure it fell between 1 and 2 mm. The previous step was repeated if the thickness was not between 1 and 2 mm. Stainless steel sample holders of rectangular shape composed of 3 parts: the core plus top and bottom covers. The core holds the 3 mm diameter sample punched from the membranes. The sample was covered by Kapton sheets, and on the top of the Kapton sheets o-rings were used to seal the sample. The top and bottom cover of the sample holder were assembled to the core with 16 screws. The samples were loaded and sealed in an argon glove box. This step was essential to avoid beam damage that caused irreproducible results if samples were loaded in air. Finally, all samples were annealed at 180 °C for 48 hours under vacuum.

The microstructure of these bulk samples was investigated with atomic force microscopy (Bruker Icon with OTESPA-R3 probe). The samples were etched using oxygen plasma at an oxygen pressure of 200

mTorr for 1 min. The sample was then heated on a heating stage at 80 °C allowing a couple minutes for the temperature to stabilize, and soft tapping-mode AFM was conducted.

Sample microstructure was also investigated using scanning electron microscopy (Thermo Fisher Scientific/FEI Dual Beam Focused Ion Beam/Field Emission Scanning Electron Microscope). For these experiments, a new set of samples were prepared since the sample required high conductivity. SEO was dissolved in chloroform solution (3% weight percentage in solution). The solution was spin coated on a silicon substrate at 1000 rpm for 30 seconds (SEO-E and SEO-I) or quiescently casted (SEO-C). The coated membranes were vapor annealed using benzene for 24 hours in a closed environment (SEO-E and SEO-I) or liquid annealed using water for 24 hours (SEO-C). After taping them on stubs with carbon tape, the samples were sputter coated with gold of 10 nm thickness. The different processing of SEO-C, with higher ϕ_{PS}, was required to capture the nanostructure with SEM.

X-ray photon correlation spectroscopy (XPCS) was conducted at Argonne National Laboratory at the 8-ID-I beamline of the Advanced Photon Source. More details of the beamline operation are reported by Sinha et al.[64] After centering the sample with the beam, each measurement was collected at a different location to minimize damage from the beam. The average scattering intensity variation over a single acquisition was less than 5% and the 1D SAXS profile remained invariant over the course of each measurement, indicating that there is no detectable radiation-induced sample damage.

III. Result

A. Structural Analysis

The 1D SAXS results at 100 °C of a representative sample of each case is shown in Figure 2. The corresponding 2D SAXS patterns are shown in panel (d). Characteristic scattering patterns for the two different processing techniques are displayed together for each sample. The slow (UD) and fast (OA) evaporation rate casting processes both showed similar scattering intensity in all samples. SEO-E UD samples exhibited sharper peaks compared to SEO-E OA. This indicates that SEO-E UD samples exhibit either longer range ordering and/or sharper domain interfaces than SEO-E OA. Changes in peak shapes with processing conditions were less significant in the other BCPs.

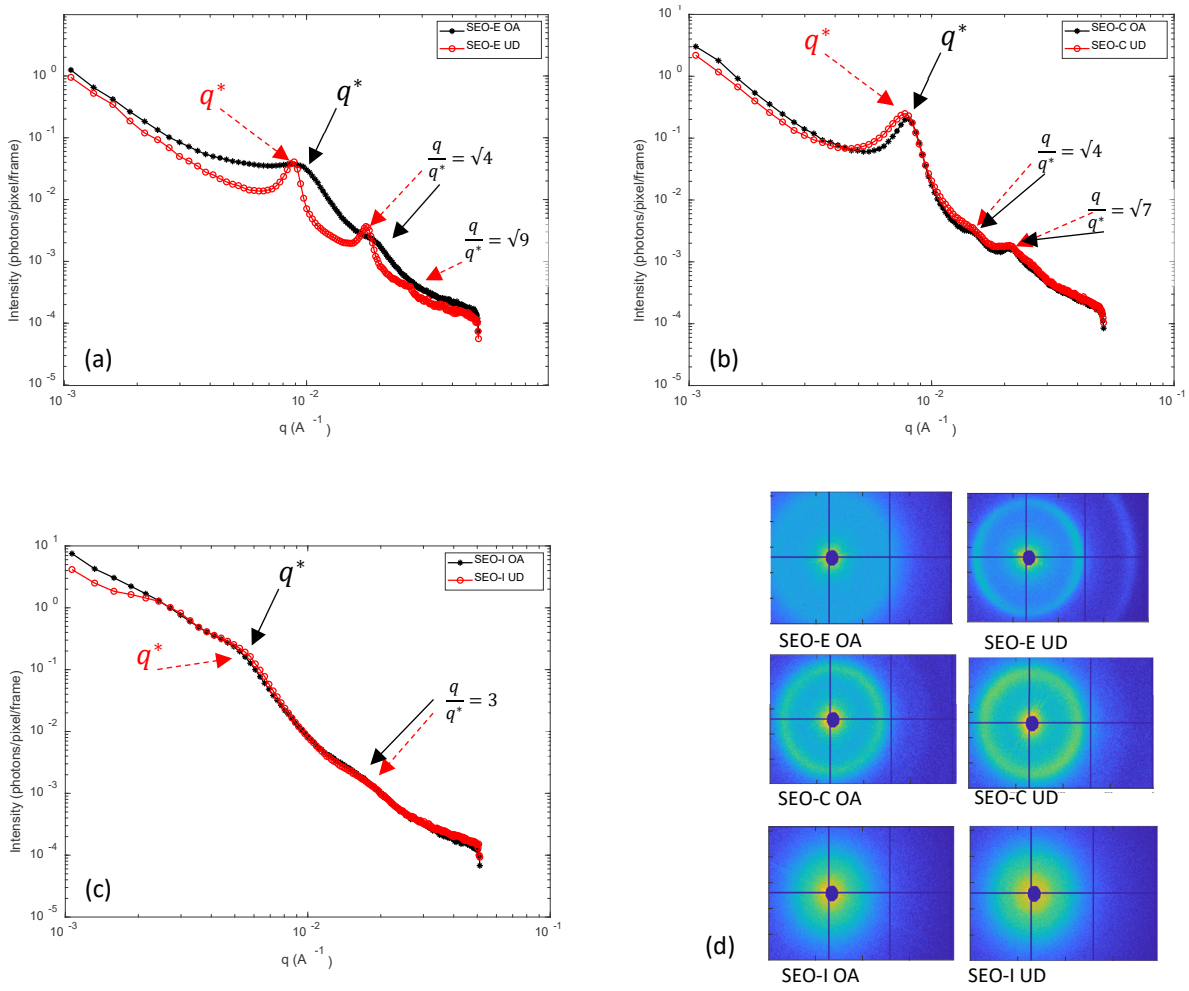

Figure 2. 1D SAXS at 100°C of (a) SEO-E casted open to air (OA) and under dish (UD), (b) SEO-C casted OA and UD, and (c) SEO-I casted OA and UD; (d) 2D SAXS pattern of SEO-E (OA and UD), SEO-C (OA and UD), and SEO-I (OA and UD).

To determine the domain size, the grain size, and the structure of each sample, the peak locations and the full width at half maximum (FWHM) of the primary scattering peak were determined. The results are reported in Table 2, where q^*, q_2, and q_3 are the locations of the primary, secondary, and tertiary peaks, respectively. The tertiary peak could not be identified for SEO-E OA, and the secondary peak was absent in SEO-I OA and SEO-I UD. SEO-E appears to exhibit a cylindrical structure due to $\frac{q_2}{q^*} = \sqrt{4}$ and $\frac{q_3}{q^*} = \sqrt{9}$. SEO-C also exhibits cylindrical structure due to $\frac{q_2}{q^*} = \sqrt{4}$ and $\frac{q_3}{q^*} = \sqrt{7}$, based on predicted peak spacing for cylindrical morphology reported by Hamely et al.[65] SEO-I is lamellar due to $\frac{q_3}{q^*} = 3$ with roughly symmetric phases that suppresses even order peaks. Our past experience with lamellar SEO BCPs has always found an absence of $\frac{q_2}{q^*} = 2$, even in somewhat lower molecular weight samples with sharper peaks.[17, 52, 66] Thus, we have assigned SEO-C cylindrical morphology, even though the peak spacing is also commensurate with predicted SAXS peak spacing of lamellar morphology.

Table 2. Structural analysis based on peak locations.

Sample	q^* (Å^{-1})	$\frac{q_2}{q^*}$	$\frac{q_3}{q^*}$	Morphology
SEO-E OA	0.00944	$\frac{0.0196}{0.0094} \cong \sqrt{4}$	-	Cylindrical
SEO-E UD	0.00888	$\frac{0.0176}{0.0089} \cong \sqrt{4}$	$\frac{0.0269}{0.0089} \cong \sqrt{9}$	Cylindrical
SEO-C OA	0.00804	$\frac{0.0148}{0.0080} \cong \sqrt{4}$	$\frac{0.0212}{0.0080} \cong \sqrt{7}$	Cylindrical
SEO-C UD	0.00776	$\frac{0.0148}{0.0078} \cong \sqrt{4}$	$\frac{0.0212}{0.0078} \cong \sqrt{7}$	Cylindrical
SEO-I OA	0.00523	-	$\frac{0.0146}{0.0052} \cong 3$	Lamellar
SEO-I UD	0.00551	-	$\frac{0.0165}{0.0055} \cong 3$	Lamellar

The domain size, d, and the grain size are calculated for all the samples at all temperatures collected, where the domain size is equal to $\frac{2\pi}{q^*}$ for lamellar, and $\frac{4\pi}{q^*\sqrt{3}}$ for cylindrical. Grain size is calculated as demonstrated by equation 1 where $FWHM$ is the full width at half the maximum of the primary peak.

$$Grain\ Size = \frac{2\pi}{FWHM} \quad (1)$$

$FWHM$ is calculated by subtracting a second order polynomial baseline to remove scattering effects innate to the apparatus. This corrected data was then fitted to a Gaussian distribution. Table 3 shows the average of the domain size and grain size at all the temperatures. Figures S1 and S2 in the Supporting Information (SI) shows the average domain size and average grain size as a function of temperature. Neither had any apparent trend with temperature. From Table 3, SEO-E is PS cylinders in PEO majority matrix, the grains size of SEO-E UD is almost double the size of SEO-E OA, and the domain size increased on the order of 10%. The changes in domain and grain size are much more modest for SEO-C and SEO-I. This suggests that low solvent evaporation rate leads to formation of somewhat larger grains and slight increase of domain size in SEO of PEO majority. When the matrix of SEO is PS, the grain size produced from low solvent evaporation rate (SEO-I UD and SEO-C UD) are slightly smaller than that of high evaporation rate (SEO-I OA and SEO-C OA). This indicates that toluene annealing is ineffective at modifying grain size significantly in PS-majority SEO.

Table 3. Structural parameters averaged over all temperatures collected. Blue is PS. Red is PEO.

Block copolymer	d_{SAXS} (nm)	$d_{predicted}$ (nm)[a]	Grain Size (SAXS) (nm)	Morphology
SEO-E OA	75 ± 1	86 ± 11	206 ± 11	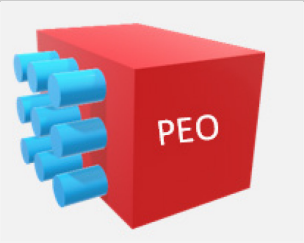
SEO-E UD	83 ± 2	86 ± 11	395 ± 28	
SEO-C OA	92 ± 2	71 ± 9	314 ± 15	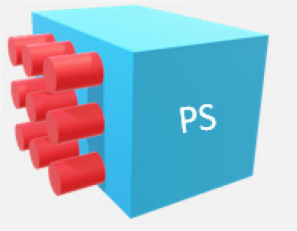
SEO-C UD	95 ± 1	71 ± 9	281 ± 9	
SEO-I OA	119 ± 1	106 ± 13	317 ± 25	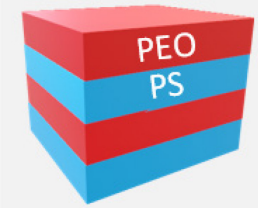
SEO-I UD	111 ± 1	106 ± 13	260 ± 14	

[a]Based on $d_{predicted} = \alpha b N^{1/2}$, where $\alpha = 2.4$ to 3.1.[67] The statistical segment lengths were taken as $b_{PS} = 0.68$ nm and $b_{PEO} = 0.61$ nm.[68] Chemical monomers were used to calculate degree of polymerization, $N = \frac{M_{PS}}{M_{styrene}} + \frac{M_{PEO}}{M_{ethylene\ oxide}}$.

As shown in Table 3, our results are in reasonable agreement with theoretical prediction of BCP domain size, with the exception of SEO-C. Moreover, the molecular weight scaling of domain sizes reported in this study agree with other literature reports of PS-b-PEO BCPs.[69, 70] The large variability of domain sizes observed here is also in agreement with these literature reports. In particular, the importance of etching out-of-equilibrium surface layers in order to observed bulk morphological structure agrees with that found by Rejek et al. It is interesting that the expected effect of solvent annealing on domain and grain sizes was only observed in SEO-E, which is the BCP with the largest rubbery PEO fraction. On the other hand, despite using a good solvent for PS, its glassy nature could not be overcome with solvent annealing and slow evaporation had a negligible (or even slightly detrimental) effect on grain size. Rejek et al. also observed that during film solution processing, the microstructure is solidified by the vitrification of PS, when the majority of the BCP is PS. In contrast, they found that when PEO forms the majority of the BCP there is sufficient mobility during film solution processing for evolution of the structure.[70] Specifically, they studied different PEO volume fractions (f_{PEO}) starting from 0.17 to 0.8 casted in two different

solvents, n-methyl-2-pyrrolidone (NMP, PEO favorable) and toluene (PS favorable). The two solvents resulted in the same morphology for each f_{PEO}.[70]

Scanning electron microscopy was used as a secondary means to confirm the structure of the BCPs. Figure 3 (a) shows SEO-E of PS cylinders (dark dots) in PEO matrix (light surface), confirming the results observed by SAXS Figure 2 (a). The SEO-C structure shown in Figure 3 (b) appears to be cylindrical with the majority of the cylinders lying in the plane of the membrane. This confirms (though not unequivocally) the cylindrical morphology assignment based on SAXS Figure 2(b). The SEO-I structure shown in Figure 3 (c) is rather poorly ordered and similar to other reports of poorly organized lamellar BCPs.[71] This poorly ordered lamellar structure is generally referred to as a bicontinuous morphology, which tends to result from BCPs that form strong membranes. This SEM result agrees with the broad peaks and odd integer peak spacing observed with SAXS Figure 2 (c).

AFM was used as a tertiary means to study the relationship between domain size and evaporation rate. Figure S3 in the SI shows AFM micrographs of all samples in this study. Lighter regions are the softer PEO phase, and the darker regions are the glassy PS phase. Figure S3 (a) and (b) are the structure of SEO-E OA and UD, respectively. Based on SAXS analysis, SEO-E is PS cylinders in PEO matrix. AFM confirms SAXS, where the black circles are PS cylinders. SEO-C UD and OA are shown in Figure S3 (c) and (d) and confirm SAXS results that SEO-C comprises PEO cylinders in a PS matrix. The PEO cylinders are seen as white circular shapes. Finally, SEO-I has a lamellar structure based on the SAXS analysis, and lamella are clearly seen in Figure S3 (e) and (f). It was notable how SEO-I Figure S4 (in SI) showed a honeycomb structure is formed (before etching) due to two facts: the slow evaporation and that toluene is a nonpolar polystyrene-selective solvent. This unique structure is produced through the selective stretching of PS. This was also observed in Navarro et al.[72]

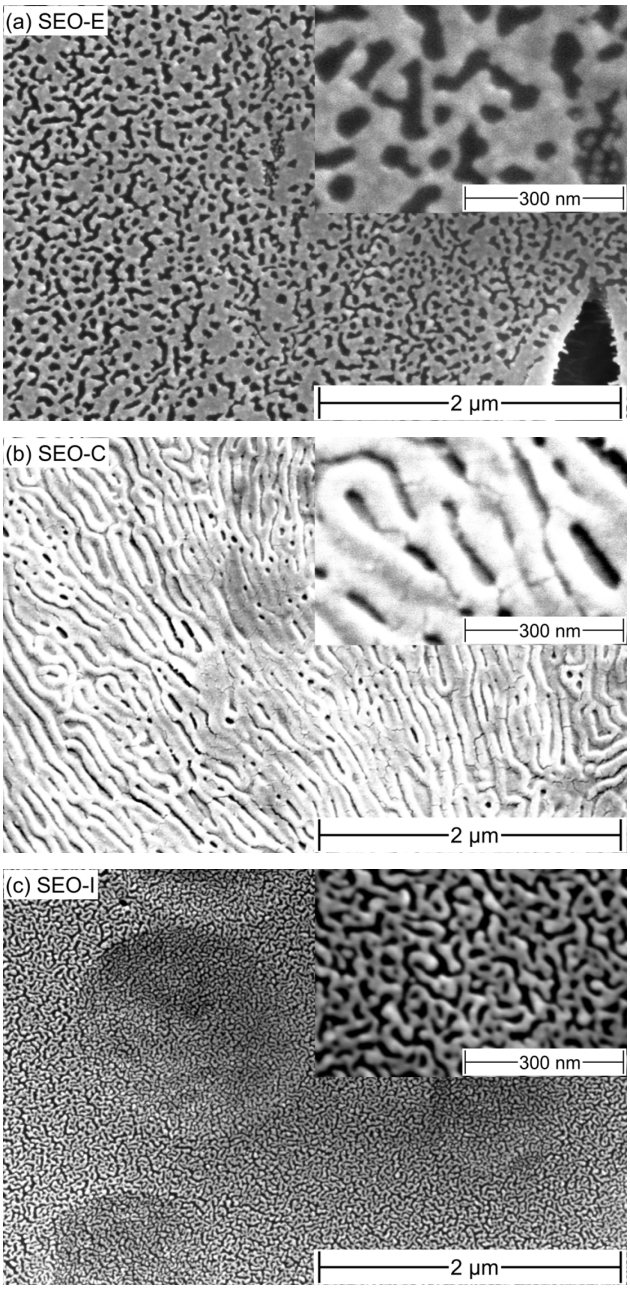

Figure 3. Scanning electron microscopy (SEM) in secondary electron mode using Everhart Thornley detector. Magnification is 50,000x (350,000x in insets). (a) SEO-E PS cylinder in PEO matrix [10 kV accelerating voltage, 0.05 nA current, and 11.5 mm working distance (WD)] ; (b) SEO-C PEO cylinders in PS matrix [5 kV, 0.20 nA, and 6.7 mm WD]; (c) SEO-I PS majority lamellae [10 kV, 0.40 nA, and 4.3 mm WD].

B. Dynamics Study

The normalized intensity autocorrelation function, g_2, is determined using the algorithm documented in previous work.[52] The resulting g_2 can be described using a stretched/compressed exponential function:[73]

$$g_2 = 1 + Ae^{-2\left[\frac{t}{\tau(q)}\right]^{\beta}} \qquad (2)$$

A is related to the speckle contrast of the experimental setup, τ is the relaxation time, and β is the exponential argument indicating if the exponential decay function is stretched ($\beta < 1$) or compressed ($\beta > 1$). The results of XPCS measurements for representative samples of each kind are shown in Figure 4. The g_2 is plotted as a function of the delay time, t, on a log scale at temperatures of 180, 160, 140, 120, and 100 °C. g_2 at different q locations are shown for all the samples in Figures S5-S10. In Figure 4, g_2 at the q value just less than the primary scattering peak, q^*, is shown. The contrast of the measurements at 180 and 160°C differs from others in all measurements because the collection of these two measurements was made at different beam times, where the instrument calibration and beam stop location were slightly different. Data at 120 and 140 °C were collected at both beam times in order to confirm that results could be quantitatively compared.

Figure 4 (a) and (b) show g_2 obtained from SEO-E, where SEO-E is PS cylinders in PEO matrix. Figure 4 (a) shows the dynamics of SEO-E OA, which exhibits a complete g_2 decay to 1 and decreasing rate with decreasing temperature. Figure 4 (b) shows the dynamics of SEO-E UD, which has the same temperature dependence as SEO-E OA and similar dynamics. As discussed below, this is despite its larger grain size compared to SEO-E OA. Figures S5 and S6 in the Supporting Information show g_2 of SEO-E OA and UD, respectively, at different q locations including those in Figure 4.

Intensity correlation functions of SEO-C OA and SEO-C UD are presented in Figure 4 (c) and (d), respectively. In PS-majority SEO-C, g_2 does not fully decay at the lowest temperatures investigated. The decay is complete at higher temperature and the rate increases with increasing temperature. Figures S7 and S8, show g_2 of SEO-C OA and UD, respectively, at different q locations including those in Figure 4.

Comparing the PEO cylinders in PS, Figure 4 (c), and PS cylinders in PEO, Figure 4 (a), casted at high evaporation rate, a full decay is observed at 100 °C observed in Figure 4 (a) SEO-E OA but cannot be seen in Figure 4 (c) SEO-C OA. This temperature is below the T_g of PS. The same behavior is observed for the slow evaporation rate casted BCP samples: SEO-E UD and SEO-C UD. The glassy nature of the PS phase provides mechanical strength, which dominates viscoelastic behavior of SEO when PS is the majority species. A comparison of viscoelastic behavior between pure PS and SEO was made by Oparaji et al., where the presence of the PEO in SEO led to a shear modulus lower than PS but rheological behavior similar to PS due to the continuous PS phase.[52] This is not the case for SEO-E in which a continuous PS phase is not present. During sample preparation it was noted that this sample is able to flow above PEO T_m and below PS T_g. Hence, much faster dynamics of the structure is observed for this sample as compared to that of the PS-majority samples.

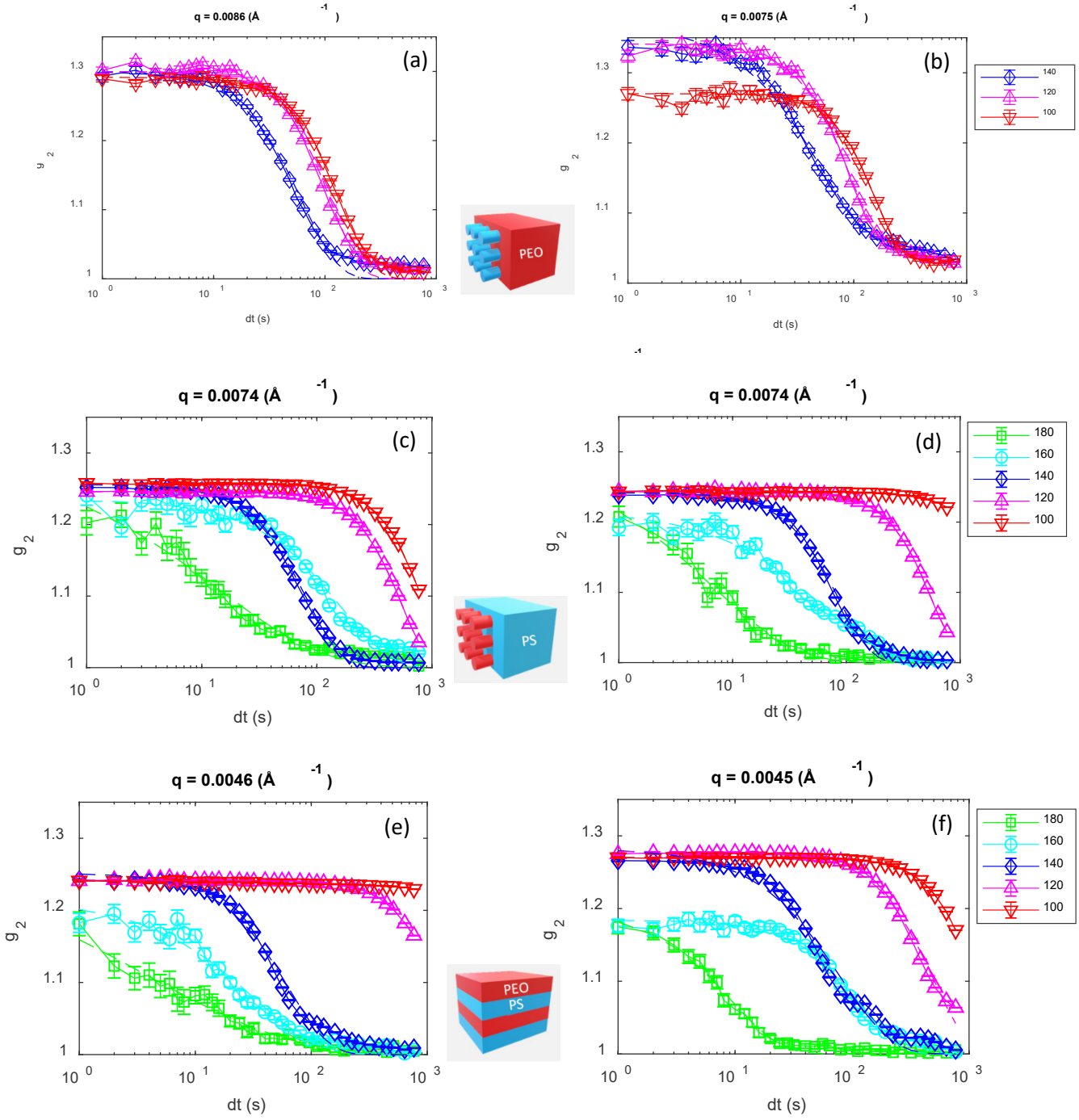

Figure 4. Autocorrelation functions obtained from SEO at q values just less than q* for (a) SEO-E OA and (b) SEO-E UD (PS cylinders in PEO); (c) SEO-C OA and (d) SEO-C UD (PEO cylinders in PS); (e) SEO-I OA and (f) SEO-I UD (PS majority lamellae). The dashed lines represent the KWW fits (equation 2) whereas the solid lines connect the data points for clarity.

Figures 4 (e) and (f) show the autocorrelation function obtained from SEO-I, lamellar block copolymer (PS majority). These samples exhibit trends similar to other samples with clear temperature dependence that is in agreement with our prior work.[52] Figures S9 and S10, show g_2 of SEO-I OA and UD, respectively, at

different q locations including those in Figure 4. Oparaji et al. studied the effect of salt on the structural dynamics of strongly segregated BCPs using the same protocols as our OA samples. The PS majority lamellar results of SEO-I OA can thus be compared to Oparaji et al.[52] in the case where r = 0 (no salt); see Table 4. A full decay of g_2 to 1 is observed in results of both Oparaji et al. and those of SEO-I OA at 180, 160, and 140 °C. At 120 °C, Oparaji et al. observed full decay of g_2 to 1, but SEO-I OA did not show significant decay at this temperature. As shown in Table 4, the PS M_n and volume fraction of SEO-I are both notably larger than the SEO of the literature report. On the other hand, the grain size of the 2 samples is equal statistically. It would appear that the smaller PS molecular weight and lower volume fraction results in significantly faster structural relaxation in the SEO used by Oparaji et al. as compared to that reported in this work. Note however, that the dominant influence of the PS block is lost at a temperature sufficiently above its T_g, i.e. 180 °C, where the 2 samples have approximately the same relaxation time.

Table 4. Lamellar sample comparison between results of Oparaji et al. at $q^* = 0.046$ Å^{-1} and SEO-I OA, at q* = 0.053 Å^{-1}. Structural relaxation times (τ_{st}) are reported at the temperatures noted in °C.

	ϕ_{PS}[a]	$M_n(PS)$ (kg/mol)	$M_n(PEO)$ (kg/mol)	τ_{st} (s) (180)	τ_{st} (s) (160)	τ_{st} (s) (140)	τ_{st} (s) (120)	Grain size (nm)	d (nm)
Oparaji (r=0) [52]	0.55	133	114	23 ± 1	81 ± 1	139 ± 1	162 ± 1	312 ± 17	162 ± 5
SEO-I OA	0.58	149	117	18 ± 3	122 ± 4	195 ± 2	531 ± 6	317 ± 25	119 ± 1

[a] at 90 °C

The dependence of the structural relaxation time, τ_{st}, on q (where q is between 0.001 and 0.01 Å^{-1}) is shown in Figures S11-S16 for the different samples studied in this work. The figures show structural relaxation times only for temperatures where there is a decay to 1. To easily compare among the results, the data are fit to a power law: $\tau_{st} = v\, q^h$. The resulting value of h is shown in Table S2. The q-dependence of τ_{st} is also presented in Figure S17 with q^* marked for reference. For SEO-E, structural relaxation rate monotonically increases with increasing temperature at all q values investigated and the q-dependence is similar for both processing methods at these temperatures, i.e. h maintains a value of approximately -1. Structural relaxation rate of SEO-C UD also increases monotonically with increasing temperature and follows power law q-dependence. However, SEO-C OA exhibits curvature in the log-log plots of τ_{st} versus q, and structural relaxation is slower at 160 °C than it is at 140 °C. Further investigation is needed to understand this behavior. The q-dependence of the structural relaxation of SEO-C is qualitatively the same for both processing methods; h increases more or less monotonically from a value less than -2 at 180 °C to greater than 0 at 120 °C. In a similar fashion, the q-dependence of SEO-I weakens with decreasing temperature from a value of h around -2 at 180 °C to a value not statistically different from 0 at 120 °C. The temperature dependence of τ_{st} is monotonic (faster at higher temperature) for SEO-I OA, but for SEO-I UD the rate is slower at 160 °C than at 140 °C. In summary, in nearly all cases h increases with decreasing temperature and in most cases τ_{st} does as well. Similar results were reported by Oparaji et al. where the structural relaxation time increased with decreasing temperature, albeit with a weaker temperature-dependence than that of entanglement relaxation from rheology measurements. They also reported very slight increase in h with decreasing temperature and values of approximately -1 that are indicative of ballistic dynamics.[52]

Figure 5 (a) shows the structural relaxation time as a function of PS volume fraction, ϕ_{PS}, for all samples at $q \cong q^*$. The structural relaxation times of SEO-E OA and SEO-E UD are quite similar at all temperatures

investigated, including 120 °C shown in Figure 5. Note that the grain size of SEO-E UD is two times larger than SEO-E OA, so the structural relaxation time is not affected by the grain size at temperatures of 140 °C and below, as shown in Figure S18. On the other hand, it is apparent from this representation that τ_{st} is a strong function of ϕ_{PS} at 120 °C, regardless of processing method. XPCS measurements at 160 and 180 °C are reported at larger ϕ_{PS} values, and τ_{st} clearly decreases with increasing temperature, but the dependence on processing method is stronger at these temperatures than is the dependence on ϕ_{PS}. At both of these temperatures the τ_{st} of OA samples increase with ϕ_{st}, but UD samples exhibit the opposite behavior. The sheer dependence of τ_{st} on ϕ_{PS} suggests that PS properties dominate the structural relaxation. The fact that this dependence is retained in the OA processing method that causes more rapid vitrification of PS suggests that a far-from-equilibrium state, such as a glassy microphase kinetically trapped in a condition with high free volume, is at the root of the structural dynamics in OA samples and in all samples near PS T_g. This does not explain dynamics in UD samples at high temperature, far from PS T_g. Comparing the structural properties of the samples from Table 3, for SEO-I ($\phi_{PS} = 0.58$) the faster OA sample has larger domains and larger grains than UD, whereas for SEO-C ($\phi_{PS} = 0.70$) the faster UD sample has larger domains but smaller grains than OA. If these trends are connected to a structural parameter, it must be domain size, where it appears that larger domains result in faster structural dynamics, as shown in Figure 5 (b). This is also true across studies as shown in Table 4. Note that in all cases the SAXS domain sizes are larger than predicted, such that larger domains are further from equilibrium, which could be expected to drive faster dynamics.

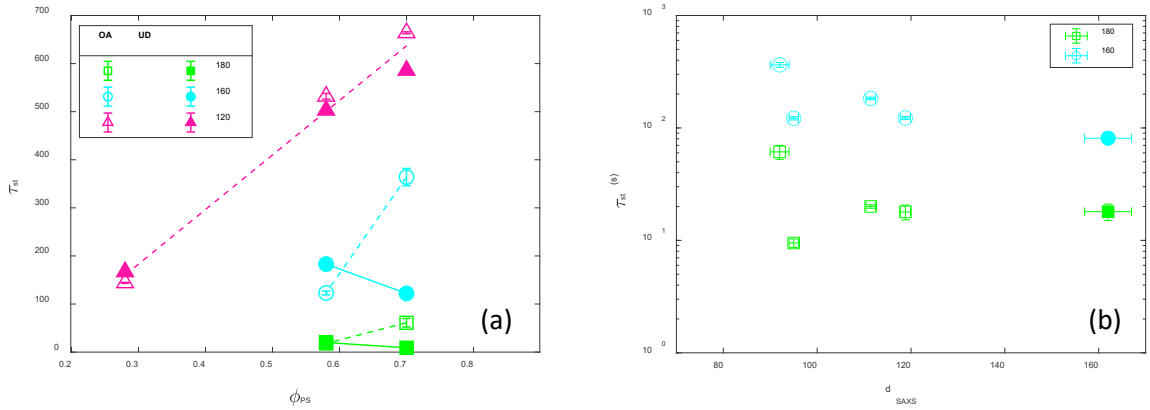

Figure 5. (a) Structural relaxation time, τ_{st} (s), as a function of PS volume fraction, ϕ_{PS} for key temperatures and with processing conditions denoted in legend. For clarity, results at 140 and 100 °C are omitted. (b) Structural relaxation time, τ_{st}, as a function of domain size d_{SAXS} at 160 and 180°C. The filled symbols in (b) are data from reference 52.

In addition to τ_{st}, the stretching exponent, β, is one of the adjustable parameters of equation 2 that was fit to the data of Figure 4. As shown in Figure S19 and Table S3, β is independent of q, but it increases with decreasing temperature. The temperature dependence is in agreement with results of Oparaji et al. for a lamellar PS majority SEO[52] and those of Ruegg et al. for a BCP/homopolymer blend.[74] In other words, the autocorrelation function shifts from stretched ($\beta < 1$) exponential decay at 180 °C and 160°C to compressed ($\beta > 1$) exponential decay at 140 and 120 °C. Figure S20 (a) shows the stretching exponent, β, as an Arrhenius function of temperature at q^* for all samples. At 180 °C all the samples express a

stretched exponent, which is indicative of diffusive behavior. At 160 °C, SEO-I OA and SEO-C UD had $0.5 < \beta < 1$, SEO-I UD and SEO-C OA had $1 < \beta < 1.5$. For the rest of the temperatures, 140, 120, and 100 °C, $\beta > 1$ for all samples. Oparaji et al. [52] described this behavior as cooperative ($\beta > 1$) hyperdiffusive motion ($h < -2$), where they defined hyperdiffusive motion by relating mean square displacement to time: $q^{-1} \sim \langle x^2 \rangle^{\frac{1}{2}} \cong t^n$. If $n = 1/2$ the behavior is diffusive, if $n > 1/2$ the behavior is hyperdiffusive. [52] Of course, for a log-log plot of τ_{st} versus q, this translates to a slope, h, of -2 for diffusive behavior and $h > -2$ for hyperdiffusive behavior. Different systems show hyperdiffusive behavior, such as jammed soft materials, colloidal gels, glass forming liquids, and polymers.[75-79] Hyperdiffusive motion can be caused by the diffusion of solvent molecules in a glassy polymer that is plasticized by the solvent. It can also be due to an extra driving force beyond random thermal motion such as residual stress within a material or interfacial energy in non-equilibrium BCP microphase-separated states.[52] Stretched exponential behavior ($\beta < 1$) has been found in liquid-like systems, while solid-like systems have been found to dynamically behave in compressed exponential manner ($1 < \beta$).[80]

The stretching exponent, β, averaged over all q's of all the samples as a function of temperature is plotted on the left axis of Figure 6. On the right axis of Figure 6, the averaged h of all the samples is plotted as a function of temperature. The black dotted line at $\beta = 1$ shows the border between compressed and stretched. The red dotted line at $h = -2$ shows the border between hyperdiffusive and diffusive behavior. The stretching exponent, β, decreases from 1.7 to 0.5 with increasing temperature from 100 to 180°C, and h also decreases from -1 to -2.5 with increasing temperature. A linear fit to β between 120 and 180°C is shown as a dashed black line. It intersects the compressed-stretched boundary at 153°C. It is interesting to find different dynamical behavior in a single system, where they are mostly observed in different systems. A compressed behavior ($\beta > 1$) is observed in colloidal glasses,[75, 81-88] gels,[78, 89-93] metallic glasses,[94, 95] polymeric systems,[96-98] and ceramics.[99] In contrast, a stretched behavior ($\beta < 1$) is observed in isolated icosahedra[80] and glass-forming systems in the liquid state.[80] Combining the two behaviors in the same system has been observed in BCP/homopolymer blends, hard colloids, and metallic glasses.[74, 80, 100] Concentration of microgels affects dynamics as measured by XPCS in an analogous way to how inverse temperature affects structural dynamics of our microphase separated nanostructure. At 180 °C, well above PS glass transition temperature, the chains move freely, leading to a stretched exponent. As PS glass transition temperature is approached, e.g. 120 °C, chains start to be trapped in their microphase structure (lamella or cylinders) and this arrested state results in cooperative, ballistic motion.

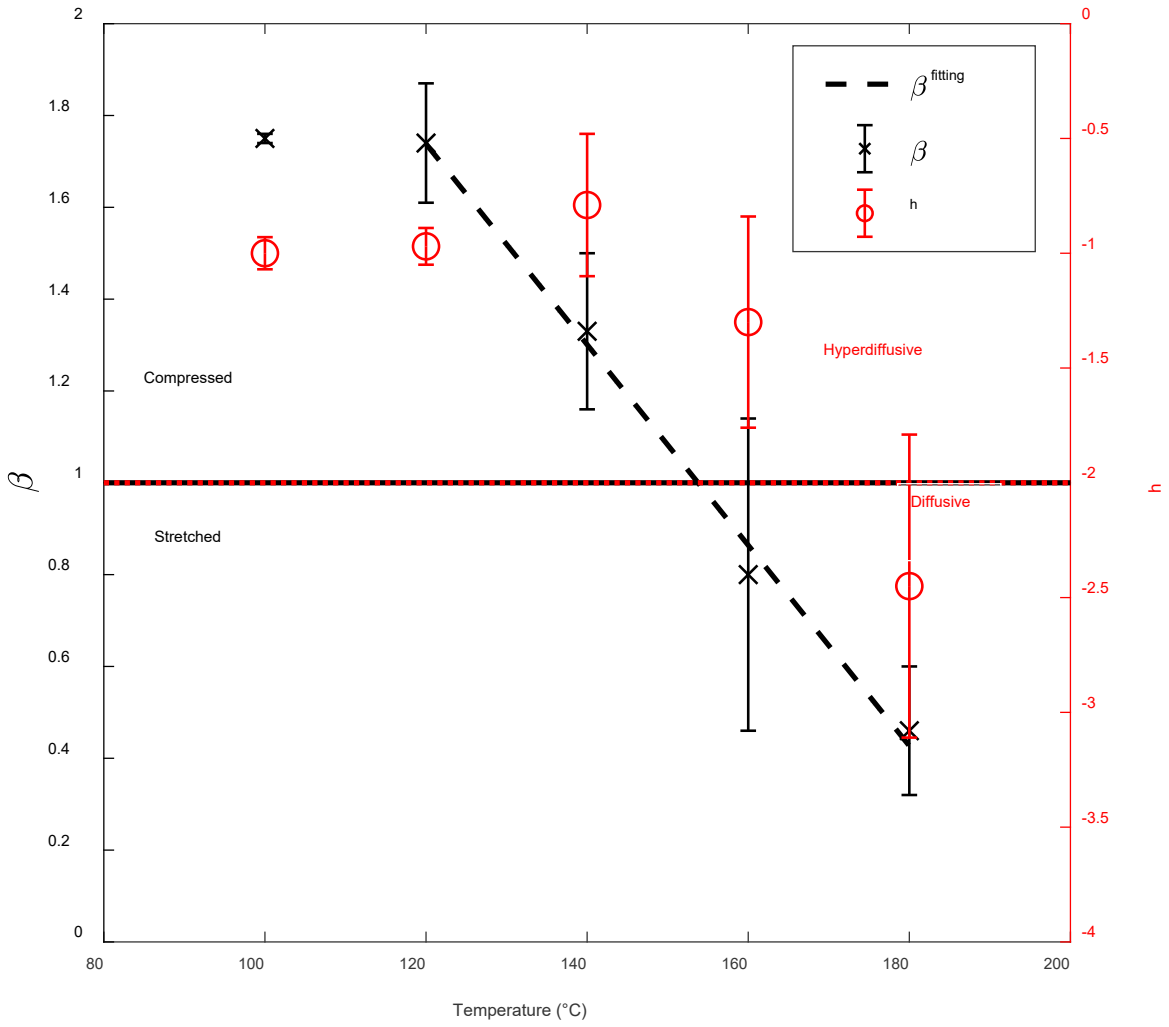

Figure 6. Stretching exponent, β, (left axis, black) and power of q-dependence of τ_{st}, h, (right axis, red). Both dependent variables are averaged over all q's and all samples. The horizontal black line denotes the boundary between compressed and stretched exponential decay behavior. Likewise, the horizontal red dotted line denotes the boundary between hyperdiffusive and diffusive dynamics. The black dashed line is a linear regression to β between 120 and 180 °C. It intersects the boundary at 153 °C or 1.13 T_g (K).

Discussion

Processing-dependent trends seen at high temperature in Figure 5 indicate that OA samples exhibit far from equilibrium dynamics of the PS phase, possibly with some kinetically trapped phase mixing. In other words, we speculate that rapid vitrification of the PS phase locks it in a high free volume state that explains why larger domains result in faster dynamics and higher ϕ_{PS} results in slower dynamics at all temperatures investigated. Note that the slowing of dynamics with increasing ϕ_{PS} is lost at 160 and 180 °C for UD samples. Rather surprisingly, structural dynamics of UD samples are actually faster than OA

samples in several cases, especially when the temperature is sufficiently far above T_g. The observed processing dependence suggests that the observed domain size dependence is not a result of confinement. It also indicates that although the far from equilibrium state of the PS phase explains the ϕ_{PS} dependence near T_g and in OA samples, it does not explain why closer to equilibrium UD samples are faster than OA samples at sufficiently high temperature.

Along similar thought process, the compressed, hyperdiffusive dynamics observed near T_g is a soft glassy behavior dominated by the volume fraction of PS in the sample. Such compressed, hyperdiffusive dynamics have been observed in other out-of-equilibrium systems, such as sheared colloids.[101] It is the out-of-equilibrium nature of the PS phase of the BCP itself that our results implicate in the observed hyperdiffusive, compressed exponential dynamics. The connection between PS microphase properties and structural dynamics is in agreement with other reports. For example, Horvat et al. used time-resolved AFM and simulations to show that correlated defect motion is connected to chain mobility.[102] Rheological properties of SEO have also been shown to be dominated by the PS block, i.e. the PS block dominates chain mobility.[52]

IV. Conclusion

This work showed that solvent evaporation rate only affects grain size weakly and in the rubbery majority BCP. In addition, this study evaluated the structural relaxation time for diblock copolymers of different morphologies: SEO-E (PS cylinders in PEO matrix), SEO-C (PEO cylinders in PS matrix), and SEO-I (PS majority lamellar) using XPCS. Structural dynamics were not found to be a function of grain size, but they are a clear function of temperature, as shown in Figure S20 (b). Dynamics were observed to become diffusive at sufficiently high temperature. The stretching exponent, β, is independent of q, but is a function of temperature. The power of the q-dependence of the structural relaxation time, h, is also a function of temperature. Both parameters decrease from compressed and hyperdiffusive at 120 °C to stretched and diffusive at 180 °C.

At 180 and 160°C far from PS glass transition, the structural relaxation time correlates with processing conditions and domain size, where larger domain samples relaxed faster than smaller domain samples. At temperatures 140, 120, and 100 °C close to PS glass transition, the structural relaxation time is dependent on the PS volume fraction regardless of processing conditions. SEO-E, with the lowest volume fraction of PS, relaxed fastest, whereas SEO-C, with the highest PS content, relaxed slowest. This clear and definitive trend has not been reported previously for structural relaxation of neat BCPs from XPCS measurements. It indicates that, at least near PS T_g, the properties of the PS phase dominate structural dynamics.

Acknowledgments

The authors acknowledge support from NSF CAREER award number 1751450. The authors thank the FAMU-FSU College of Engineering Machine shop for fabrication of XPCS sample holders, Dr. Hannah Pimentel for assistance conducting SEM, as well as Daniel Barzycki and Dr. Ralm Ricarte for advice regarding processing SEM samples. This research used resources of the Advanced Photon Source, a U.S. Department of Energy (DOE) Office of Science User Facility operated for the DOE Office of Science by Argonne National Laboratory under Contract DE-AC02-06CH11357.

References

[1] P. P. Soo, B. Huang, Y.-I. Jang, Y.-M. Chiang, D. R. Sadoway, A. M. Mayes, *J. Electrochem. Soc.* **1999**, *146*, 32.
[2] M. Singh, O. Odusanya, G. M. Wilmes, H. B. Eitouni, E. D. Gomez, A. J. Patel, V. L. Chen, M. J. Park, P. Fragouli, H. Iatrou, N. Hadjichristidis, D. Cookson, N. P. Balsara, *Macromolecules* **2007**, *40*, 4578.
[3] G. M. Stone, S. A. Mullin, A. A. Teran, D. T. Hallinan, Jr., A. M. Minor, A. Hexemer, N. P. Balsara, *Journal of the Electrochemical Society* **2012**, *159*, A222.
[4] D. T. Hallinan, S. A. Mullin, G. M. Stone, N. P. Balsara, *J. Electrochem. Soc.* **2013**, *160*, A464.
[5] S. Choudhury, R. Mangal, A. Agrawal, L. A. Archer, *Nature Communications* **2015**, *6*.
[6] J. L. Nugent, S. S. Moganty, L. A. Archer, *Adv. Mater.* **2010**, *22*, 3677.
[7] Y. Wang, A. P. Sokolov, *Current Opinion in Chemical Engineering* **2015**, *7*, 113.
[8] S. Mogurampelly, V. Sethuraman, V. Pryamitsyn, V. Ganesan, *The Journal of Chemical Physics* **2016**, *144*, 154905.
[9] R. Bouchet, T. N. T. Phan, E. Beaudoin, D. Devaux, P. Davidson, D. Bertin, R. Denoyel, *Macromolecules* **2014**, *47*, 2659.
[10] A. S. Arico, P. Bruce, B. Scrosati, J. M. Tarascon, W. Van Schalkwijk, *Nature Materials* **2005**, *4*, 366.
[11] S. Cheng, D. M. Smith, Q. Pan, S. Wang, C. Y. Li, *RSC Advances* **2015**, *5*, 48793.
[12] O. Kim, G. Jo, Y. J. Park, S. Kim, M. J. Park, *Journal of Physical Chemistry Letters* **2013**, *4*, 2111.
[13] N. S. Schauser, K. J. Harry, D. Y. Parkinson, H. Watanabe, N. P. Balsara, *J. Electrochem. Soc.* **2015**, *162*, A398.
[14] H. Odani, K. Taira, N. Nemoto, M. Kurata, *Polymer Engineering & Science* **1977**, *17*, 527.
[15] D. S. Simmons, *Macromol. Chem. Phys.* **2016**, *217*, 137.
[16] H. Watanabe, *PLASTICS ENGINEERING-NEW YORK-* **1998**, *46*, 317.
[17] O. Oparaji, M. Minelli, C. Zhu, E. Schaible, A. Hexemer, D. T. Hallinan Jr, *Polymer* **2017**, *120*, 209.
[18] M. Minelli, M. G. Baschetti, D. T. Hallinan, Jr., N. P. Balsara, *Journal of Membrane Science* **2013**, *432*, 83.
[19] H. Hu, M. Gopinadhan, C. O. Osuji, *Soft matter* **2014**, *10*, 3867.
[20] S. B. Darling, *Prog. Polym. Sci.* **2007**, *32*, 1152.
[21] M. Luo, T. H. Epps III, *Macromolecules* **2013**, *46*, 7567.
[22] Y. Lin, A. Böker, J. He, K. Sill, H. Xiang, C. Abetz, X. Li, J. Wang, T. Emrick, S. Long, Q. Wang, A. Balazs, T. P. Russell, *Nature* **2005**, *434*, 55.
[23] A. A. Leniart, P. Pula, E. H. R. Tsai, P. W. Majewski, *Macromolecules* **2020**, *53*, 11178.
[24] C. Sinturel, M. Vayer, M. Morris, M. A. Hillmyer, *Macromolecules* **2013**, *46*, 5399.
[25] Y. S. Jung, C. A. Ross, *Nano Letters* **2007**, *7*, 2046.
[26] W. Bai, A. F. Hannon, K. W. Gotrik, H. K. Choi, K. Aissou, G. Liontos, K. Ntetsikas, A. Alexander-Katz, A. Avgeropoulos, C. A. Ross, *Macromolecules* **2014**, *47*, 6000.
[27] X. Gu, I. Gunkel, A. Hexemer, T. P. Russell, *Macromolecules* **2016**, *49*, 3373.
[28] X. Zhang, B. C. Berry, K. G. Yager, S. Kim, R. L. Jones, S. Satija, D. L. Pickel, J. F. Douglas, A. Karim, *ACS Nano* **2008**, *2*, 2331.
[29] S. O'Driscoll, G. Demirel, R. A. Farrell, T. G. Fitzgerald, C. O'Mahony, J. D. Holmes, M. A. Morris, *Polym. Adv. Technol.* **2011**, *22*, 915.
[30] X. Zhang, J. F. Douglas, R. L. Jones, *Soft Matter* **2012**, *8*, 4980.
[31] P. Pula, A. Leniart, P. W. Majewski, *Soft Matter* **2022**, *18*, 4042.
[32] M. Chintapalli, X. C. Chen, J. L. Thelen, A. A. Teran, X. Wang, B. A. Garetz, N. P. Balsara, *Macromolecules* **2014**, *47*, 5424.
[33] L. S. Grundy, S. Fu, M. D. Galluzzo, N. P. Balsara, *Macromolecules* **2022**.

[34] M. W. Matsen, F. S. Bates, *Macromolecules* **1996**, *29*, 1091.
[35] M. Doi, S. F. Edwards, "*The Theory of Polymer Dynamics*", Oxford University Press, USA, 1986, p. 408.
[36] C. Iacob, J. Runt, *ACS Macro Letters* **2016**, *5*, 476.
[37] M. Krutyeva, A. Wischnewski, M. Monkenbusch, L. Willner, J. Maiz, C. Mijangos, A. Arbe, J. Colmenero, A. Radulescu, O. Holderer, M. Ohl, D. Richter, *Phys. Rev. Lett.* **2013**, *110*, 108303.
[38] A. K. Jha, S. L. Tsang, A. E. Ozcam, R. D. Offeman, N. P. Balsara, *Journal of Membrane Science* **2012**, *401*, 125.
[39] "*Thermoplastic Elastomers A Comprehensive Review*", Hanser Publishers, New York, 1987, p. 574.
[40] Y. Xue, Q. Zhang, W. Wang, H. Cao, Q. Yang, L. Fu, *Advanced Energy Materials* **2017**, *7*, 1602684.
[41] D. Deng, K. Novoselov, Q. Fu, N. Zheng, Z. Tian, X. Bao, *Nature nanotechnology* **2016**, *11*, 218.
[42] W. Li, J. Liu, D. Zhao, *Nature Reviews Materials* **2016**, *1*, 1.
[43] V. Ganesan, V. Pyramitsyn, C. Bertoni, M. Shah, *ACS Macro Letters* **2012**, *1*, 513.
[44] M. S. Alshammasi, F. A. Escobedo, *Macromolecules* **2018**.
[45] O. Taleb, D. C. Barzycki, C. G. Polanco, R. G. Ricarte, D. Hallinan, *Int. J. Heat Mass Transfer* **2022**, *188*, 122631.
[46] S. P. Gido, J. Gunther, E. L. Thomas, D. Hoffman, *Macromolecules* **1993**, *26*, 4506.
[47] H. Jinnai, K. Yasuda, T. Nishi, *Macromolecular Symposia* **2006**, *245-246*, 170.
[48] M. D. Ediger, *Annu. Rev. Phys. Chem.* **2000**, *51*, 99.
[49] M. T. Cicerone, F. R. Blackburn, M. D. Ediger, *J. Chem. Phys.* **1995**, *102*, 471.
[50] A. J. Patel, S. Mochrie, S. Narayanan, A. Sandy, H. Watanabe, N. P. Balsara, *Macromolecules* **2010**, *43*, 1515.
[51] I. Sikharulidze, I. P. Dolbnya, A. Fera, A. Madsen, B. I. Ostrovskii, W. H. de Jeu, *Physical review letters* **2002**, *88*, 115503.
[52] O. Oparaji, S. Narayanan, A. Sandy, S. Ramakrishnan, D. Hallinan, *Macromolecules* **2018**, *51*, 2591.
[53] T. Thurn-Albrecht, W. Steffen, A. Patkowski, G. Meier, E. W. Fischer, G. Grübel, D. Abernathy, *Physical review letters* **1996**, *77*, 5437.
[54] A. Malik, A. Sandy, L. Lurio, G. Stephenson, S. Mochrie, I. McNulty, M. Sutton, *Physical review letters* **1998**, *81*, 5832.
[55] R. M. Lewis III, H. K. Beech, G. L. Jackson, M. J. Maher, K. Kim, S. Narayanan, T. P. Lodge, M. K. Mahanthappa, F. S. Bates, *ACS Macro Letters* **2018**, *7*, 1486.
[56] R. H. Colby, "Block Copolymers, Melt Rheology of", in *Encyclopedia of Materials: Science and Technology*, K.H.J. Buschow, R.W. Cahn, M.C. Flemings, B. Ilschner, E.J. Kramer, S. Mahajan, and P. Veyssière, Eds., Elsevier Science Ltd., 2001727.
[57] J. H. Rosedale, F. S. Bates, *Macromolecules* **1990**, *23*, 2329.
[58] K. A. Koppi, M. Tirrell, F. S. Bates, K. Almdal, R. H. Colby, *Journal De Physique Ii* **1992**, *2*, 1941.
[59] M. Rubinstein, S. P. Obukhov, *Macromolecules* **1993**, *26*, 1740.
[60] H. Hahn, J. H. Lee, N. P. Balsara, B. A. Garetz, H. Watanabe, *Macromolecules* **2001**, *34*, 8701.
[61] J. M. Sebastian, C. Lai, W. W. Graessley, R. A. Register, G. R. Marchand, *Macromolecules* **2002**, *35*, 2700.
[62] N. Hadjichristidis, H. Iatrou, S. Pispas, M. Pitsikalis, *Journal of Polymer Science Part A: Polymer Chemistry* **2000**, *38*, 3211.
[63] M. W. Matsen, *The European Physical Journal E* **2009**, *30*, 361.
[64] S. K. Sinha, Z. Jiang, L. B. Lurio, *Advanced Materials* **2014**, *26*, 7764.
[65] I. W. Hamley, V. Castelletto, *Progress in polymer science* **2004**, *29*, 909.
[66] O. Oparaji, X. Zuo, D. T. Hallinan Jr, *Polymer* **2016**, *100*, 206.
[67] E. Helfand, Z. R. Wasserman, *Macromolecules* **1976**, *9*, 879.
[68] P. C. Hiemenz, T. P. Lodge, "*Polymer chemistry*", CRC press, 2007.
[69] C. Huang, Y. Zhu, X. Man, *Physics Reports* **2021**, *932*, 1.

[70] T. Rejek, P. Schweizer, D. Joch, L. Portilla, E. Spiecker, M. Halik, *Macromolecules* **2020**, *53*, 5604.
[71] L. M. Pitet, M. A. Amendt, M. A. Hillmyer, *Journal of the American Chemical Society* **2010**, *132*, 8230.
[72] L. Navarro, A. F. Thünemann, D. Klinger, *ACS Macro Letters* **2022**, *11*, 329.
[73] H. Guo, G. Bourret, R. B. Lennox, M. Sutton, J. L. Harden, R. L. Leheny, *Physical review letters* **2012**, *109*, 055901.
[74] M. L. Ruegg, A. J. Patel, S. Narayanan, A. R. Sandy, S. G. J. Mochrie, H. Watanabe, N. P. Balsara, *Macromolecules* **2006**, *39*, 8822.
[75] M. Bellour, A. Knaebel, J. Harden, F. Lequeux, J.-P. Munch, *Physical review E* **2003**, *67*, 031405.
[76] C. Caronna, Y. Chushkin, A. Madsen, A. Cupane, *Physical review letters* **2008**, *100*, 055702.
[77] C.-H. Cheng, K. Kamitani, S. Masuda, K. Uno, N. Dechnarong, T. Hoshino, K. Kojio, A. Takahara, *Polymer* **2021**, *229*, 124003.
[78] L. Cipelletti, S. Manley, R. Ball, D. Weitz, *Physical review letters* **2000**, *84*, 2275.
[79] T. Hoshino, D. Murakami, Y. Tanaka, M. Takata, H. Jinnai, A. Takahara, *Physical Review E* **2013**, *88*, 032602.
[80] Z. W. Wu, W. Kob, W.-H. Wang, L. Xu, *Nature communications* **2018**, *9*, 1.
[81] R. Bandyopadhyay, D. Liang, H. Yardimci, D. A. Sessoms, M. A. Borthwick, S. G. Mochrie, J. L. Harden, R. L. Leheny, *Physical Review Letters* **2004**, *93*, 228302.
[82] F. Schosseler, S. Kaloun, M. Skouri, J. Munch, *Physical Review E* **2006**, *73*, 021401.
[83] R. Angelini, L. Zulian, A. Fluerasu, A. Madsen, G. Ruocco, B. Ruzicka, *Soft Matter* **2013**, *9*, 10955.
[84] R. Angelini, E. Zaccarelli, F. A. de Melo Marques, M. Sztucki, A. Fluerasu, G. Ruocco, B. Ruzicka, *Nature communications* **2014**, *5*, 4049.
[85] P. Kwaśniewski, A. Fluerasu, A. Madsen, *Soft Matter* **2014**, *10*, 8698.
[86] R. Angelini, A. Madsen, A. Fluerasu, G. Ruocco, B. Ruzicka, *Colloids and Surfaces A: Physicochemical and Engineering Aspects* **2014**, *460*, 118.
[87] R. Angelini, B. Ruzicka, *Colloids and Surfaces A: Physicochemical and Engineering Aspects* **2015**, *483*, 316.
[88] R. Pastore, G. Pesce, M. Caggioni, *Scientific reports* **2017**, *7*, 1.
[89] B. Chung, S. Ramakrishnan, R. Bandyopadhyay, D. Liang, C. Zukoski, J. Harden, R. Leheny, *Physical review letters* **2006**, *96*, 228301.
[90] H. Guo, S. Ramakrishnan, J. L. Harden, R. L. Leheny, *The Journal of chemical physics* **2011**, *135*, 154903.
[91] D. Orsi, L. Cristofolini, G. Baldi, A. Madsen, *Physical review letters* **2012**, *108*, 105701.
[92] L. Cristofolini, *Current opinion in colloid & interface science* **2014**, *19*, 228.
[93] B. W. Mansel, M. A. Williams, *Soft Matter* **2015**, *11*, 7016.
[94] B. Ruta, Y. Chushkin, G. Monaco, L. Cipelletti, E. Pineda, P. Bruna, V. Giordano, M. Gonzalez-Silveira, *Physical review letters* **2012**, *109*, 165701.
[95] Z. Evenson, B. Ruta, S. Hechler, M. Stolpe, E. Pineda, I. Gallino, R. Busch, *Physical review letters* **2015**, *115*, 175701.
[96] P. Falus, M. Borthwick, S. Narayanan, A. Sandy, S. Mochrie, *Physical review letters* **2006**, *97*, 066102.
[97] R. A. Narayanan, P. Thiyagarajan, S. Lewis, A. Bansal, L. Schadler, L. Lurio, *Physical review letters* **2006**, *97*, 075505.
[98] S. Srivastava, A. Kandar, J. Basu, M. Mukhopadhyay, L. Lurio, S. Narayanan, S. Sinha, *Physical Review E* **2009**, *79*, 021408.
[99] V. Balitska, O. Shpotyuk, M. Brunner, I. Hadzaman, *Chemical Physics* **2018**, *501*, 121.
[100] V. Nigro, B. Ruzicka, B. Ruta, F. Zontone, M. Bertoldo, E. Buratti, R. Angelini, *Macromolecules* **2020**, *53*, 1596.
[101] A. Madsen, R. L. Leheny, H. Guo, M. Sprung, O. Czakkel, *New Journal of Physics* **2010**, *12*, 055001.
[102] A. Horvat, G. J. A. Sevink, A. V. Zvelindovsky, A. Krekhov, L. Tsarkova, *Acs Nano* **2008**, *2*, 1143.